Electronic Supplementary Material (ESI) for Journal of Materials Chemistry A.

Supporting information

Mixed Anion Effects on Structural and Electrochemical Characteristics of $Li_4Ti_5O_{12}$ for High-rate and Durable Anode Materials

Hye-min Kim[1,‡], Dae-wook Kim[1], Kenjiro Hara[1,‡], Hiromasa Shiiba[2], Youn Charles-Blin[1,‡], Eugenio Otal[1], Hideki Tanaka[2], Katsuya Teshima[1,2], Gabriel Sánchez-Santolino[3], Ryo Ishikawa[3], Yuichi Ikuhara[3], and Nobuyuki Zettsu* [1,2,4]

1. Department of Materials Chemistry, Shinshu University, 4-17-1 Wakasato, Nagano, 380-8553, Japan.
2. Research Initiative for Supra-Materials, Shinshu University, 4-17-1 Wakasato, Nagano, 380-8553, Japan.
3. Institute of Engineering Innovation, The University of Tokyo, Bunkyo, Tokyo 113-8656, Japan.
4. Energy Landscape Architectonics Brain Bank, Shinshu University, 4-17-1 Wakasato, Nagano, 380-8553, Japan

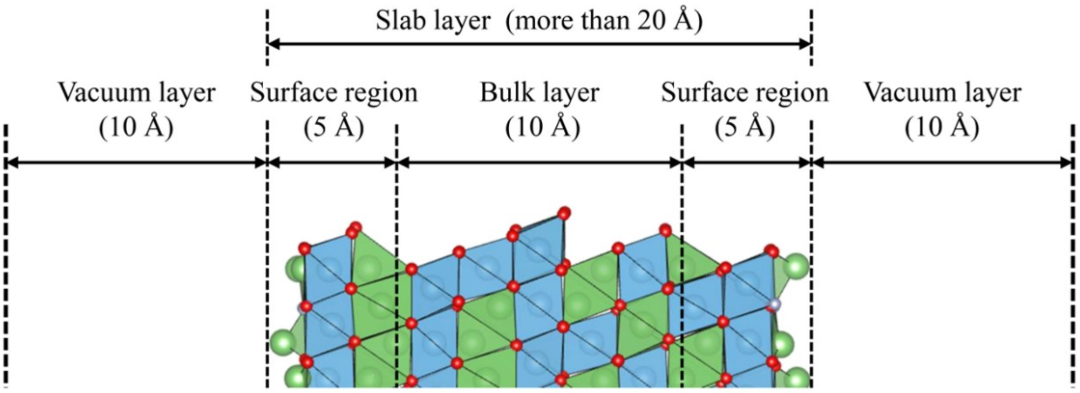

Figure S1

Schematic of the slab cell used for density functional theory (DFT) calculations. The slab cells are constructed from the relaxed bulk structure of LTO, and the lattice parameters are fixed for the slab cells. More than 20 Å slab thicknesses are chosen for all surface facets, with vacuum thicknesses of 20 Å, for accurate calculation of the surface properties.

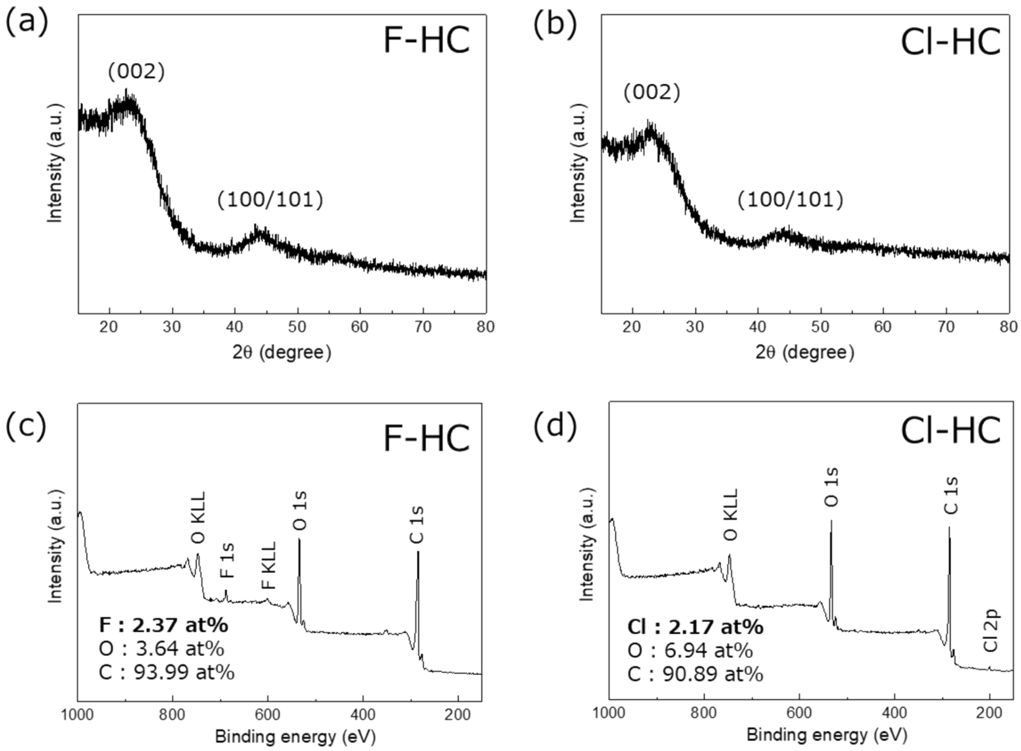

Figure S2

(a, b) XRD profiles and (c, d) XPS wide scan spectra of as synthesized F, Cl-doped heterocarbon powders.

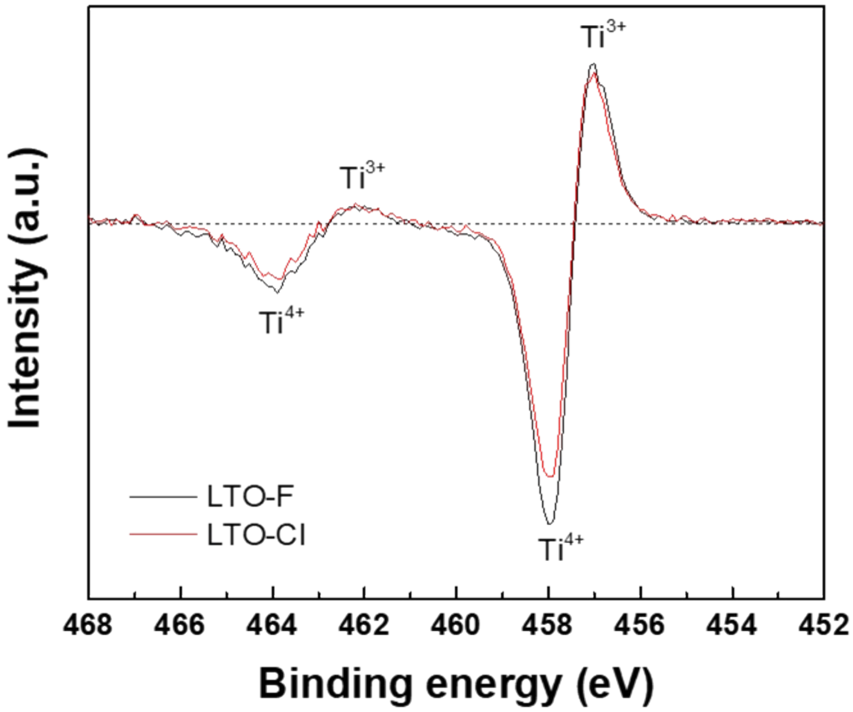

Figure S3

Difference spectrum, obtained by subtracting the normalized Ti 2p spectrum of F-LTO and Cl-LTO from that of LTO, exhibits two positive peaks at approximately 462 and 457 eV (Ti^{3+}) and two valleys at 464 and 458 eV (Ti^{4+}).

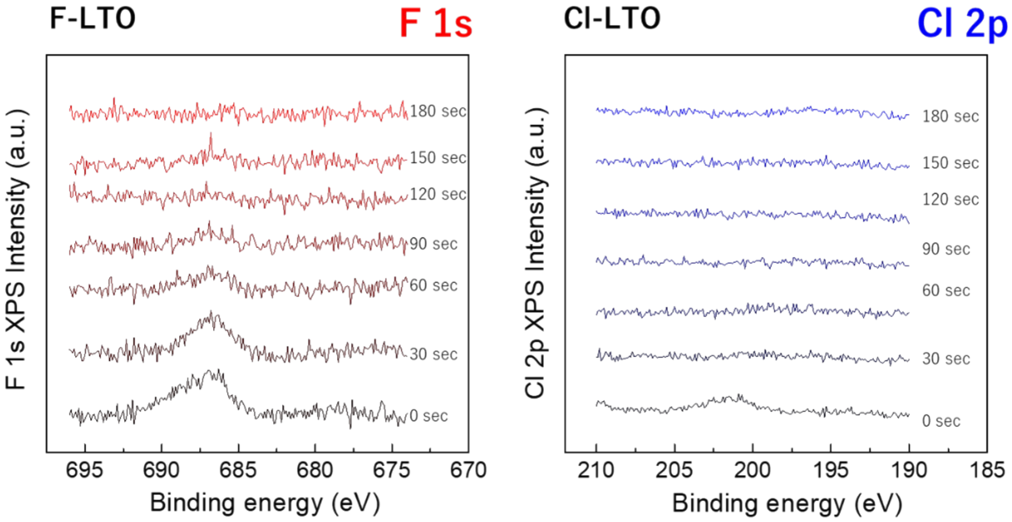

Figure S4

(a) Depth profile of F 1s core-level spectra obtained from F-LTO crystals and (b) Cl 2p core-level spectra of Cl-LTO crystals. The etching thickness is controlled at 20 nm per Ar sputtering step, which is determined relative to the silicon wafer.

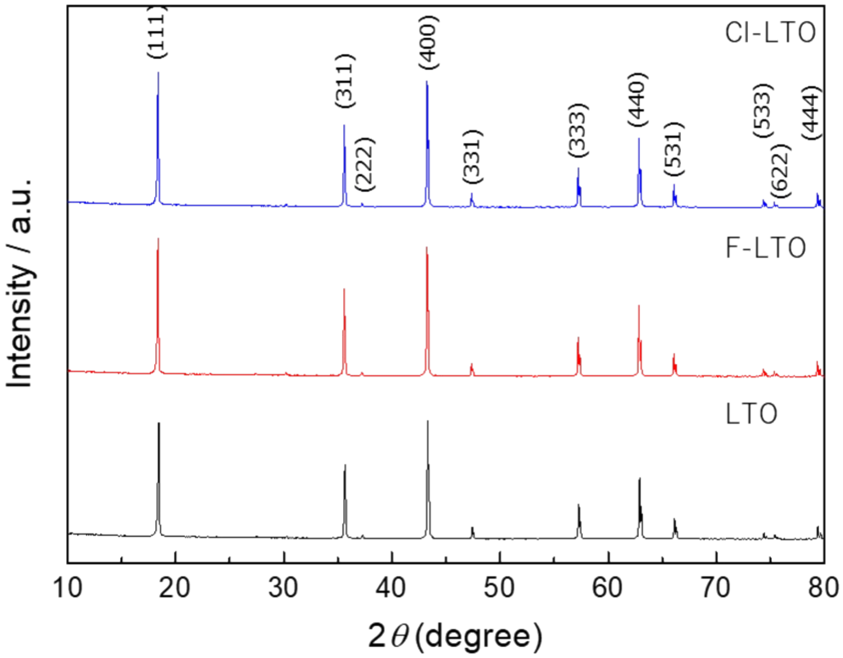

Figure S5

Powder XRD patterns for LTO, F-LTO, and Cl-LTO crystals.

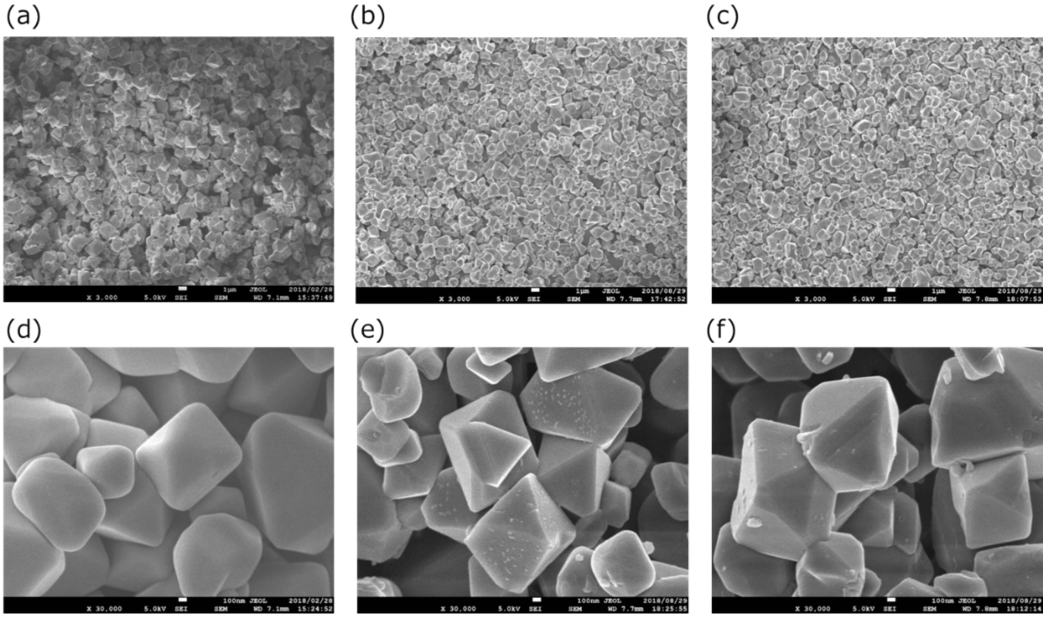

Figure S6

FE-SEM images of (a,d) LTO, (b, e) F-LTO, and (c, f) Cl-LTO crystals.

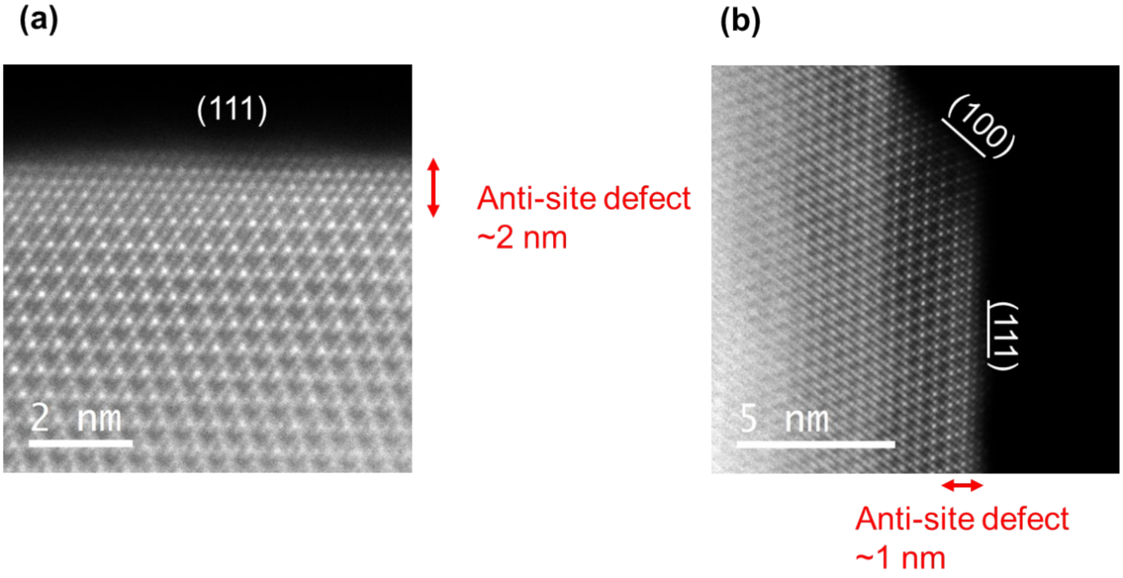

Figure S7

Surface atomic and electronic structures of halide anion doped LTOs characterized via scanning transmission electron microscopy (STEM). (a) F-LTO and (b) shows annular dark-field images of F-LTO and Cl-LTO.

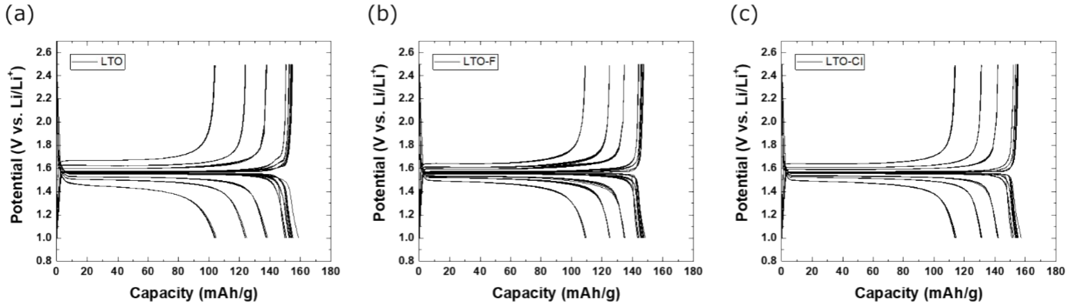

Figure S8

Galvanostatic charge-discharge profiles of LTO, F-LTO, and Cl-LTO electrodes in half-cells with various C-rates, operated under a controlled cut-off voltage range of 2.4–1.0 V (Li^+/Li).

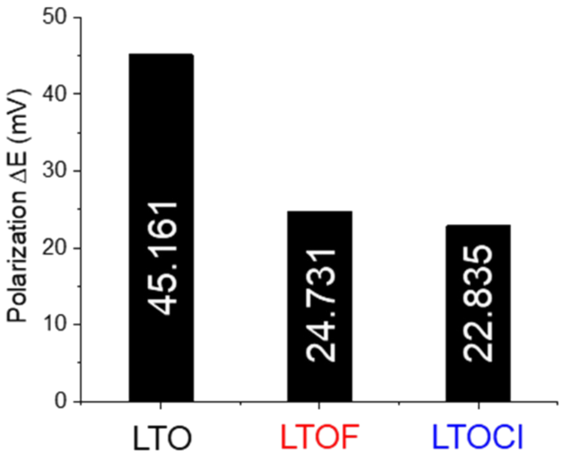

Figure S9

Peak difference between cathodic and anodic waves observed in cyclic voltammetry (CV) measurements taken from LTO, F-LTO, and Cl-LTO electrodes in Li cells.

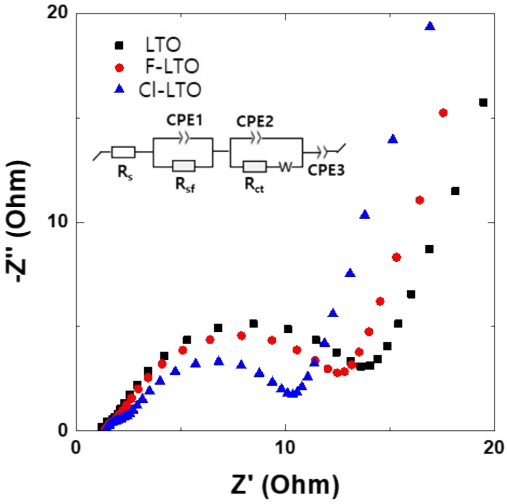

	R_s (ohm)	R_{sf} (ohm)	R_{ct} (ohm)
LTO	1.20	2.82	11.89
F-LTO	1.34	2.56	10.04
Cl-LTO	1.43	2.17	7.63

Figure S10

Nyquist plot of aged half-cells comprising LTO, F-LTO, and Cl-LTO electrodes.

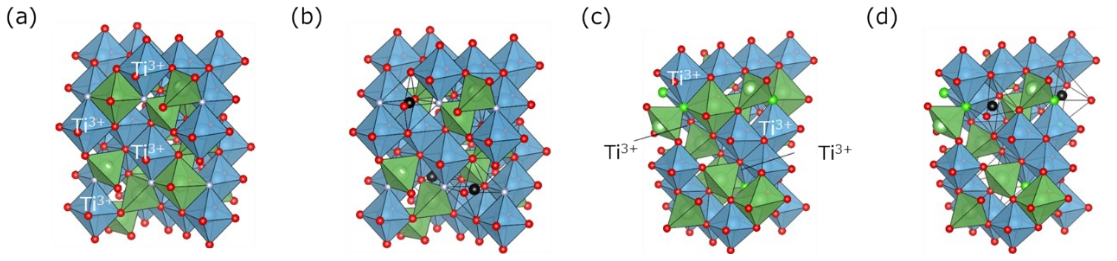

Figure S11

Stable atomic arrangements in (a, c) $Li_4Ti_5O_{11}F_1$ and (b, d) $Li_4Ti_5O_{11}Cl_1$ analyzed by density functional theory (DFT) calculations for (a, c) mixed valence model and (b, d) Li^+ deficient model. The colors correspond to the following elements: green for Li, blue for Ti, red for O, silver for F, light green for Cl, and black for Li^+ deficient.

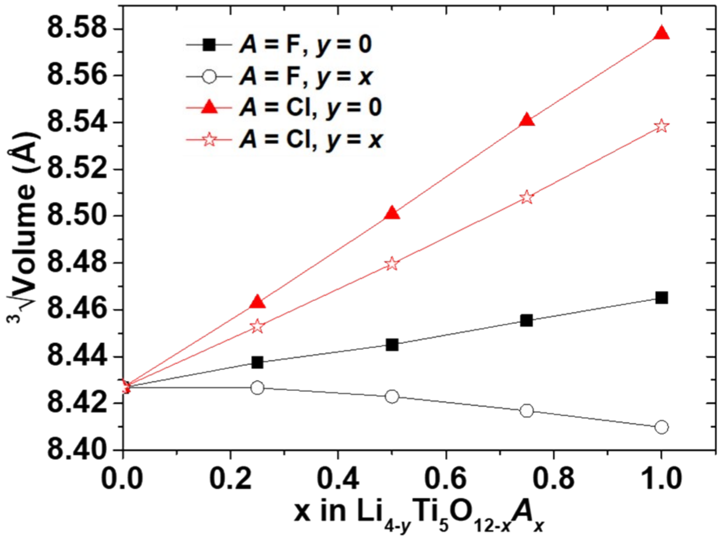

Figure S12

Lattice volume of $Li_{4-y}Ti_5O_{12-x}A_x$, determined by density functional theory (DFT) calculations, for both mixed valence and Li^+ deficient models.

Table S1

F^- substitution energy for mixed-valence model and Li^+ deficient model, evaluated using density functional theory (DFT) calculations for $Li_{4-y}Ti_5O_{12-x}F_x$.

Mixed valence model ($Ti^{4+} \rightarrow Ti^{3+}$)	ΔH [eV]
$Li_4Ti_5O_{12} + \frac{1}{4}LiF \rightarrow Li_4Ti_5O_{11.75}F_{0.25} + \frac{1}{8}Li_2O + \frac{1}{16}O_2$	0.77
$Li_4Ti_5O_{12} + \frac{1}{2}LiF \rightarrow Li_4Ti_5O_{11.50}F_{0.50} + \frac{1}{4}Li_2O + \frac{1}{8}O_2$	1.53
$Li_4Ti_5O_{12} + \frac{3}{4}LiF \rightarrow Li_4Ti_5O_{11.25}F_{0.75} + \frac{3}{8}Li_2O + \frac{3}{16}O_2$	2.29
$Li_4Ti_5O_{12} + LiF \rightarrow Li_4Ti_5O_{11}F_1 + \frac{1}{2}Li_2O + \frac{1}{4}O_2$	3.05

Li Deficient Structure ($Li^+ \rightarrow V'_{Li}$)	ΔH [eV]
$Li_4Ti_5O_{12} + \frac{1}{4}LiF \rightarrow Li_{3.75}Ti_5O_{11.75}F_{0.25} + \frac{1}{4}Li_2O$	0.59
$Li_4Ti_5O_{12} + \frac{1}{2}LiF \rightarrow Li_{3.50}Ti_5O_{11.50}F_{0.50} + \frac{1}{2}Li_2O$	1.18
$Li_4Ti_5O_{12} + \frac{3}{4}LiF \rightarrow Li_{3.25}Ti_5O_{11.25}F_{0.75} + \frac{3}{4}Li_2O$	1.74
$Li_4Ti_5O_{12} + LiF \rightarrow Li_3Ti_5O_{11}F_1 + Li_2O$	2.30

Table S2

Cl^- substitution energy for mixed-valence model and Li^+ deficient model, evaluated using density functional theory (DFT) calculations for $Li_{4-y}Ti_5O_{12-x}Cl_x$.

Mixed valence model ($Ti^{4+} \rightarrow Ti^{3+}$)	**ΔH [eV]**
$Li_4Ti_5O_{12} + \frac{1}{4}LiCl \rightarrow Li_4Ti_5O_{11.75}Cl_{0.25} + \frac{1}{8}Li_2O + \frac{1}{16}O_2$	0.91
$Li_4Ti_5O_{12} + \frac{1}{2}LiCl \rightarrow Li_4Ti_5O_{11.50}Cl_{0.50} + \frac{1}{4}Li_2O + \frac{1}{8}O_2$	1.80
$Li_4Ti_5O_{12} + \frac{3}{4}LiCl \rightarrow Li_4Ti_5O_{11.25}Cl_{0.75} + \frac{3}{8}Li_2O + \frac{3}{16}O_2$	2.71
$Li_4Ti_5O_{12} + LiCl \rightarrow Li_4Ti_5O_{11}Cl_1 + \frac{1}{2}Li_2O + \frac{1}{4}O_2$	3.58

Li Deficient Structure ($Li^+ \rightarrow V'_{Li}$)	**ΔH (eV)**
$Li_4Ti_5O_{12} + \frac{1}{4}LiCl \rightarrow Li_{3.75}Ti_5O_{11.75}Cl_{0.25} + \frac{1}{4}Li_2O$	0.70
$Li_4Ti_5O_{12} + \frac{1}{2}LiCl \rightarrow Li_{3.50}Ti_5O_{11.50}Cl_{0.50} + \frac{1}{2}Li_2O$	1.39
$Li_4Ti_5O_{12} + \frac{3}{4}LiCl \rightarrow Li_{3.25}Ti_5O_{11.25}Cl_{0.75} + \frac{3}{4}Li_2O$	2.10
$Li_4Ti_5O_{12} + LiCl \rightarrow Li_3Ti_5O_{11}Cl_1 + Li_2O$	2.71

Table S3

Chemical potential of oxygen gas at which the formation energy of the mixed-valence model is equal to that of the Li^+-deficient model. This indicates the phase transition energy from a mixed-valence structure to a Li^+-deficient structure in $Li_{4-y}Ti_5O_{12-x}F_x$ and $Li_{4-y}Ti_5O_{12-x}Cl_x$. The chemical potential of oxygen atoms is converted to temperature under an oxygen partial pressure of 0.2 atm and at 900 K.

$Li_{4-y}Ti_5O_{12-x}F_x$

x	$\mu(O) - 1/2E(O_2)$ (eV)	Temperature at $p(O_2) = 0.2$ atm (K)	$p(O_2)$ at 900 K (Pa)
0.25	-2.92	~2210	10^{-16}
0.50	-2.77	~2100	10^{-14}
0.75	-2.97	~2240	10^{-16}
1.00	-3.00	~2260	10^{-17}

$Li_{4-y}Ti_5O_{12-x}Cl_x$

x	$\mu(O) - 1/2E(O_2)$ (eV)	Temperature at $p(O_2) = 0.2$ atm (K)	$p(O_2)$ at 900 K (Pa)
0.25	-1.71	~1370	10^{-3}
0.50	-1.67	~1340	10^{-2}
0.75	-1.62	~1300	10^{-2}
1.00	-1.73	~1380	10^{-3}

Computational studies have demonstrated that the mixed-valence model structure is more stable than the Li vacancy model due to changes in the chemical potential of oxygen gas on the right side of the chemical reaction equations presented in Tables S1 and S2. The relationship between the chemical potential of oxygen gas, temperature, and pressure is described by the following equations:

$$\mu_{O_2}\left(T, p_{O_2}\right) = \mu^0_{O_2}(T, p^0) + k_B T \ln\left(\frac{p_{O_2}}{p^0}\right)$$

$$\mu_{O_2}\left(T, p_{O_2}\right) = \mu^0_{O_2}(T, P^0) + k_B T ln\left(\frac{p_{O_2}}{p^0}\right)$$

where μ_{O2} (T, p_{O2}) represents the chemical potential of oxygen gas at a designated temperature and pressure, μ^O_{O2} (T, p^O) is the chemical potential of oxygen at temperature T and standard pressure p^O, k_B is the Boltzmann constant, and p_{O2} is the oxygen partial pressure. The following equation was obtained by converting the above equation using the total energy of oxygen gas obtained from DFT calculations:

$$\mu_{O_2}\left(T, p_{O_2}\right) = E^{\mathrm{DFT}}_{O_2} + \left(G^0_{O_2}(T) - G^0_{O_2}(0\ \mathrm{K})\right) + k_B T \ln\left(\frac{p_{O_2}}{p^0}\right)$$

$$\mu_{O_2}\left(T, p_{O_2}\right) = E^{DFT}_{O_2} + \left(G^{0}_{O_2}(T) - G^{0}_{O_2}(0\ K)\right) + k_B T ln\left(\frac{p_{O_2}}{p^0}\right)$$

where $E^{\mathrm{DFT}}{}_{O2}$ is the total energy of oxygen gas at absolute zero calculated using DFT based on a previous report. The second term on the right side corresponds to the Gibbs free energy of oxygen gas at standard pressure and the experimental values obtained from the National Institute of Standards and Technology (NIST).

Table S4

Surface energies of the {100}, {110}, and {111} facets of LTO and F-LTO for both the mixed-valence and Li^+-deficient models, as determined by density functional theory (DFT) calculations.

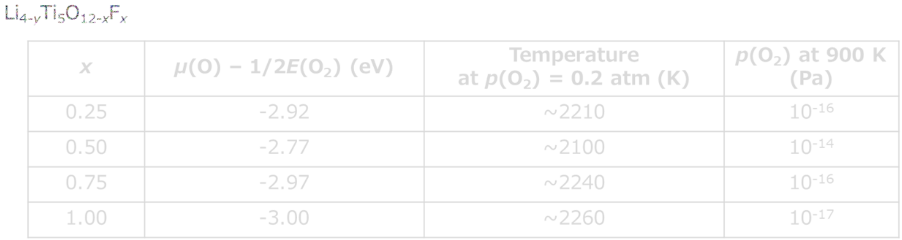

$Li_{4-y}Ti_5O_{12-x}F_x$

x	$\mu(O) - 1/2E(O_2)$ (eV)	Temperature at $p(O_2) = 0.2$ atm (K)	$p(O_2)$ at 900 K (Pa)
0.25	-2.92	~2210	10^{-16}
0.50	-2.77	~2100	10^{-14}
0.75	-2.97	~2240	10^{-16}
1.00	-3.00	~2260	10^{-17}

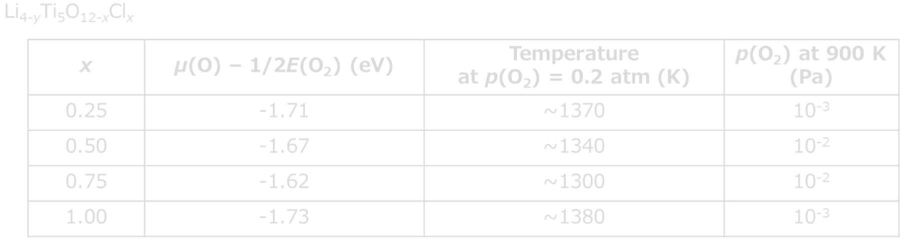

$Li_{4-y}Ti_5O_{12-x}Cl_x$

x	$\mu(O) - 1/2E(O_2)$ (eV)	Temperature at $p(O_2) = 0.2$ atm (K)	$p(O_2)$ at 900 K (Pa)
0.25	-1.71	~1370	10^{-3}
0.50	-1.67	~1340	10^{-2}
0.75	-1.62	~1300	10^{-2}
1.00	-1.73	~1380	10^{-3}

To study the surface structure, slab models with two types of structures, mixed-valence and Li^+-deficient structures, were created. A segregated structure, in which the halide ions introduced by substitution are segregated onto the crystal surface, was considered. Based on the most stable surface structure model identified for LTO, a segregated structure forming a mixed-valence model was prepared by randomly introducing halide ions into the terminal layer of the surface structure model. Furthermore, Li^+-deficient segregated structures were created by randomly introducing Li^+ defects into the mixed-valence model-segregated structures.

Table S5

Surface energies of the {100}, {110}, and {111} facets of LTO and Cl-LTO for both the mixed-valence and Li$^+$-deficient models, as determined by density functional theory (DFT) calculations.

Crystal facet		Surface energy (J·m^{-2})		
		Pure LTO	Mixed valence model in Cl-LTO	Li defect formation model In Cl-LTO
{100}	(100)	0.97	0.74	1.11
	(010)	0.84	0.73	0.53
	(001)	0.84	0.42	0.18
			0.87	1.07
{110}	(110)	0.62	0.31	
	(101)	0.61	0.29	0.15
	(011)	0.56		
{111}	(111)	0.51	0.58	0.39
	(1-11)	0.52	0.56	0.29